NORMAL-MODE ANALYSIS OF LATERAL DIFFUSION ON A BOUNDED MEMBRANE SURFACE

DENNIS E. KOPPEL
Department of Biochemistry, University of Connecticut Health Center, Farmington, Connecticut 06032

ABSTRACT The normal-mode analysis of fluorescence redistribution after photobleaching, introduced for the characterization of lateral diffusion on spherical membrane surfaces, has been generalized and extended to other surface geometries. Theoretical expressions are derived for the characteristic values and orthogonal characteristic functions of the diffusion equations for cylindrical surfaces, ellipsoids of revolution and dimpled discoidal surfaces. On the basis of these results, a simple analytical function is proposed as an empirical solution for the analysis of photobleaching data on a variety of discoidal surfaces. Special experimental and computational methods for determining the surface-diffusion coefficient are described, and demonstrated with data for lipid diffusion in erythrocyte membranes.

INTRODUCTION

In recent years, fluorescence redistribution after photobleaching (FRAP) has been widely applied to the study of lateral diffusion processes in biological membranes. (For recent reviews, see references 1–5). The technique uses brief intense laser light pulses to introduce spatially nonuniform distributions of fluorescent probe. The subsequent redistribution after bleaching is monitored with attenuated laser illumination.

The experimental and analytical approaches best employed in a given case are governed to a large extent by the sample geometry. With large, flat membranes or long filaments, one can treat the sample as infinite in extent. Employing localized spot bleaching (6, 7) or extended pattern bleaching (8–11), one models the recovery process as one-dimensional or two-dimensional diffusion in a rectangular coordinate system without outer boundaries. The general solution for the concentration distribution is a Fourier integral over the spatial Fourier components, with the spatial profile of the initial bleached spot or pattern determining the characteristic distance for diffusion.

For bounded membrane surfaces of sufficient symmetry and regularity, one can take a different approach. Taking boundary conditions into account, the general solution for the concentration reduces to a sum over discrete orthogonal characteristic functions. Suitably defined moments of the concentration distribution decay exponentially with relaxation rates proportional to diffusion coefficient D, and inversely proportional to the square of the size of the membrane. This normal-mode analysis was developed for a spherical surface (12), and applied to the measurement of diffusion on osmotically swollen and mutant spherocytic erythrocytes (13, 14), and osmotically swollen cuprizone-induced giant mitochondria (15). Here, the normal-mode analysis is extended to surfaces of other geometries. One immediate objective of this analysis is to improve the characterization of diffusion on discoidal membrane surfaces such as normal erythrocytes and sperm cell heads. Detailed experimental results will be presented elsewhere (Bürkli et al., submitted for publication).

Sections below present the following approach to the problem: The normal-mode analysis is first recast in general terms applicable to a coordinate surface of any orthogonal curvilinear coordinate system (see the section entitled General Principles). Explicit solutions are then derived for several specific geometries (see the sections entitled Cylindrical Surfaces, Ellipsoids of Revolution, and Other Discoidal Surfaces). Finally, experimental and computational methods are described, and illustrated with data on normal discoidal human erythrocytes (see the Experimental Methods and Results section).

GENERAL PRINCIPLES

We choose a system of orthogonal curvilinear coordinates ξ_1, ξ_2, ξ_3, such that the surface in question corresponds to one of the coordinate surfaces, e.g., ξ_1 = constant. The concentration of molecules on the surface, $c(\xi_2, \xi_3, t)$, is governed by the diffusion equation

$$\frac{\partial c(\xi_2, \xi_3, t)}{\partial t} = D\nabla^2 c(\xi_2, \xi_3, t) = \frac{D}{h_2 h_3}\left[\frac{\partial}{\partial \xi_2}\left(\frac{h_3}{h_2}\frac{\partial c}{\partial \xi_2}\right) + \frac{\partial}{\partial \xi_3}\left(\frac{h_2}{h_3}\frac{\partial c}{\partial \xi_3}\right)\right], \quad (1)$$

where h_2 and h_3 are scale factors for ξ_2 and ξ_3 respectively, defined so that a change $d\xi_n$ in a coordinate produces a

displacement $h_n d\xi_n$ cm along the coordinate line.[1] For simplicity, we specify further at this point that the concentration is independent of ξ_3 initially (e.g., azimuthally symmetric), so that it is a function of only ξ_2 and t for all time. For specific cases below, we will be able to relax this constraint.

Eq. 1 is solved for $c(\xi_2, t)$ by the method of separation of variables, giving the general solution

$$c(\xi_2, t) = \sum_n A_n S_n(\xi_2) e^{-Dk_n^2 t}, \tag{2}$$

where characteristic functions $S_n(\xi_2)$ and separation constants k_n^2 are solutions of a simplified Sturm-Liouville equation (reference 16, p. 719)

$$\frac{d}{d\xi_2}\left[\frac{h_3}{h_2}\frac{dS(\xi_2)}{d\xi_2}\right] + h_2 h_3 k^2 S(\xi_2) = 0. \tag{3}$$

Coefficients A_n are determined by the particular initial (postbleach) concentration distribution, $c(\xi_2, 0)$.

In the normal-mode analysis, it is not necessary to specify a particular functional form of $c(\xi_2, 0)$. Rather, we define, and measure, the ℓth moment of the distribution

$$M_\ell(t) \equiv \int c(\xi_2, t) S_\ell(\xi_2) h_2 h_3 d\xi_2. \tag{4}$$

By the orthogonality property of the characteristic functions (see Appendix), we then have

$$M_\ell(t) \alpha A_\ell e^{-Dk_\ell^2 t}. \tag{5}$$

For a general mixed population of surface molecules with different diffusion characteristics, $M_\ell(t)$ would be a sum or distribution of exponentials with weight constants proportional to the relative fluorescence intensities of the different components.

CYLINDRICAL SURFACES

We consider diffusion on the surface of a cylinder of uniform but arbitrary cross section of circumference L (see Fig. 1 *a*). We associate ξ_3 with the coordinate along the axis of the cylinder. Hence, $h_3 = 1$. ξ_2 is taken as the angular coordinate mapping the path around the cylinder, with h_2 an arbitrary function of ξ_2. It is convenient to introduce a normalized coordinate λ ($0 \le \lambda \le 1$) marking the contour length around the cylinder, so that $d\lambda = h_2 d\xi_2 / L$. Eq. 3, in this case, reduces to

$$\frac{d^2}{d\lambda^2} S(\lambda) + k^2 L^2 S(\lambda) = 0, \tag{6}$$

[1]The expression for the Laplacian in the second part of Eq. 1 is derived from the standard expression for the gradient (see reference 16, Eq. 1.4.2), coupled with the expression for the divergence on a surface, div $J = (1/h_2h_3)[\partial(h_3J_2)/\partial\xi_2 + \partial(h_2J_3)/\partial\xi_3]$, derived from the definition div $\mathbf{J} \equiv \lim_{\text{area}\to 0}[\int \mathbf{J} \cdot d\mathbf{s}/\text{area}]$, analogous to the derivation of Eq. 1.4.6 of reference 16 for three dimensions.

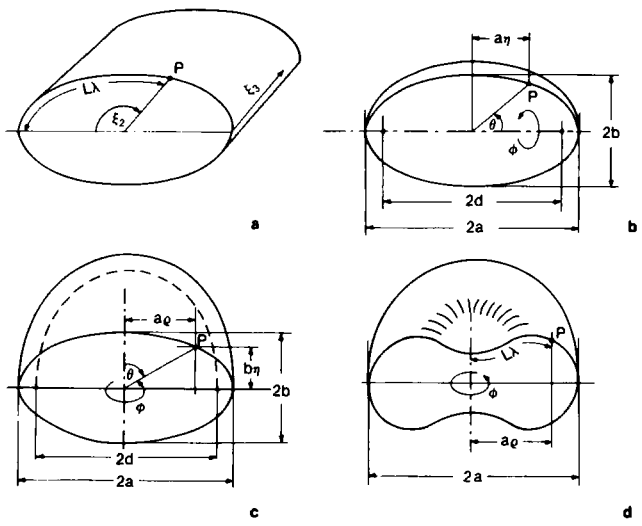

FIGURE 1 Coordinate systems introduced for various membrane geometries: (*a*) general cylindrical surface, (*b*) prolate ellipsoid of revolution, (*c*) oblate ellipsoid of revolution, (*d*) general discoidal surface.

independent of h_2; i.e., independent of the shape of the cross section. In accordance with physical intuition, this is equivalent to the problem of one-dimensional diffusion with periodic boundary conditions, giving (according to Eqs. 2 and 6)

$$c(\lambda, t) = \sum_{n=-\infty}^{\infty} A_n \exp(ik_n L\lambda - Dk_n^2 t), \tag{7}$$

with

$$k_n L = 2\pi n.$$

ELLIPSOIDS OF REVOLUTION

Consider an ellipse of eccentricity ϵ ($0 \le \epsilon \le 1$), defined as the ratio of the interfocal distance ($2d$) to the major axis ($2a$). Rotation of the ellipse about the major axis produces a prolate ellipsoid of revolution, a coordinate surface (ξ_1 = constant) of prolate spheroidal coordinates. Likewise, rotation of the ellipse about the minor axis produces an oblate ellipsoid of revolution, a coordinate surface (ξ_1 = constant) of oblate spheroidal coordinates. In both cases, the coordinate ξ_2 now corresponds to η, the normalized projection distance ($-1 \le \eta \le 1$) along the unique axis of symmetry (the major axis for prolate ellipsoids, the minor axis for oblate ellipsoids; see Figs. 1 *b, c*). ξ_3 is equated to ϕ, the azimuthal angle about this axis. We then have (reference 16, pp. 661–662)

$$h_2 = a\left[\frac{1 - \epsilon^2\eta^2}{1 - \eta^2}\right]^{1/2} \tag{8a}$$

$$h_3 = a(1 - \epsilon^2)^{1/2}(1 - \eta^2)^{1/2}, \tag{8b}$$

for prolate coordinates, and

$$h_2 = a\left[\frac{1-\epsilon^2(1-\eta^2)}{1-\eta^2}\right]^{1/2} \tag{8c}$$

$$h_3 = a(1-\eta^2)^{1/2} \tag{8d}$$

for oblate coordinates.

Eq. 1 is separable in t, η, and ϕ. The general solution is

$$c(\eta,\phi,t) = \sum_{n,m} A_{n,m} S_n^m(\eta) e^{im\phi} e^{-Dk_n^2 t}, \tag{9}$$

where $S_n^m(\eta)$ and k_n^2 are solutions of the equation

$$\frac{d}{d\eta}\left[\frac{(1-\eta^2)}{(1-\epsilon^2\eta^2)^{1/2}}\frac{dS(\eta)}{d\eta}\right] + \left[k^2a^2 - \frac{m^2}{(1-\epsilon^2)(1-\eta^2)}\right](1-\epsilon^2\eta^2)^{1/2}S(\eta) = 0, \tag{10a}$$

for prolate ellipsoids, and

$$\frac{d}{d\eta}\left[\frac{(1-\eta^2)}{[1-\epsilon^2(1-\eta^2)]^{1/2}}\frac{dS(\eta)}{d\eta}\right] + \left[k^2a^2 - \frac{m^2}{(1-\eta^2)}\right][1-\epsilon^2(1-\eta^2)]^{1/2}S(\eta) = 0. \tag{10b}$$

for oblate ellipsoids.

Limiting Cases—Spheres and Disks

To solve Eqs. 10a, b for ellipsoids of general eccentricity, we first examine the simpler solutions in certain limiting cases. As $\epsilon^2 \to 0$, keeping the major axis constant, both prolate and oblate ellipsoids become spheres of radius a. In this limit, both Eqs. 10a and 10b reduce to

$$\frac{d}{d\eta}\left[(1-\eta^2)\frac{dS}{d\eta}\right] + \left[k^2a^2 - \frac{m^2}{1-\eta^2}\right]S(\eta) = 0. \tag{11}$$

The solutions are the associated Legendre polynomials $[P_n^m(\eta)]$ with $k_n^2a^2 = n(n+1)$, as expected (12, 17, 18).

As $\epsilon^2 \to 1$, again keeping the major axis constant, oblate ellipsoids become disks of radius a. This limit is of practical interest for even functions of η, which can be expressed as functions of $\rho = (1-\eta^2)^{1/2}$, the normalized radial distance (see Fig. 1 *c*). Eq. 10b then reduces to

$$\frac{d}{d\rho}\left[\rho\frac{d}{d\rho}S(\rho)\right] + \rho\left[k^2a^2 - \frac{m^2}{\rho^2}\right]S(\rho) = 0 \tag{12}$$

in the $\epsilon^2 \to 1$ limit. The solutions are $J_m(ka\rho)$, the Bessel functions of order m (19, 20). The separation constant k is limited to the series of discrete values for which $dJ_m(ka\rho)/d\rho = 0$ at $\rho = 1$, establishing the disk boundary as impermeable to diffusion (20). For $J_o(ka\rho)$, this gives (19) $ka = 3.83, 7.02, 10.17, 13.32, \ldots$.

Approximate Solutions

Approximate solutions of Eqs. 10a, b are derived below in two different ways. Deviations from $\epsilon^2 = 0$ are incorporated into Legendre polynomial expansions of $S(\eta)$ and k^2a in powers of ϵ^2. Deviations from $\epsilon^2 = 1$ are derived through perturbation calculations. For simplicity, all further calculations are for azimuthally symmetric concentration distributions (i.e., $m = 0$ in Eqs. 9 and 10).

Legendre Polynomial Expansions

The Legendre polynomials, $P_n(\eta)$, form a complete orthogonal set on the interval $-1 \le \eta \le 1$. We can thus expand the functions $S_\ell(\eta)$ as sums of Legendre polynomials

$$S_\ell(\eta) = \sum_n{}' b_n P_n(\eta), \tag{13}$$

where the prime indicates a sum over all odd positive integers for ℓ odd, and all even nonnegative integers for ℓ even. For all $n \neq \ell$, we expand coefficients b_n in powers of ϵ^2

$$b_n/b_\ell = \sum_{h=1}^{\infty} d_{n,2h}\epsilon^{2h}, \tag{14}$$

consistent with the $\epsilon^2 \to 0$ limit (see above). Similarly, we expand k^2a^2 in power of ϵ^2, i.e.,

$$k_\ell^2a^2 = \ell(\ell+1) + \sum_{n=1}^{\infty} q_{2n}\epsilon^{2n}. \tag{15}$$

To solve for coefficients $d_{n,2h}$ and q_{2n}, substitute Eqs. 13–15 back into Eqs. 10a or 10b, and recast to the form of a double expansion

$$\sum_i{}' \sum_{j=o}^{\infty} f_{i,2j} P_i(\eta)\epsilon^{2j} = 0. \tag{16}$$

Since Eq. 16 must hold for all values of ϵ, we can set each expression for

$$g_j \equiv \sum_i{}' f_{i,2j}P_i(\eta)$$

individually to zero. Furthermore, by the orthogonality of the Legendre polynomials, we must have $f_{i,2j} = 0$, for all i and j. Expressing each $f_{i,2j}$ as analytical functions[2] of the q_{2n}'s and $d_{n,2h}$'s, and setting each to zero starting with the smallest values of i and j and progressing through all relevant i's for each value of j, we can solve for the unknown parameters sequentially. This was accomplished for the first-order prolate function, and the second-order

[2]In practice, analytical expressions were first derived for coefficients g_j in Eq. 16. Each of these is a sum of products of the unknown parameters, Legendre polynomials, and the first and second derivatives of Legendre polynomials. Expressions for $f_{i,2j}$ as functions of $\{d_{n,2h}\}$ and $\{q_{2n}\}$ were derived through numerical integration: $f_{i,2j} = [(2i+1)/2]\int_{-1}^{1}$.

prolate and oblate functions for all terms up to the order of ϵ^8. The numerical results are listed in Table I.

The solid curves in Figs. 2–5 are theoretical values of $k_\ell^2 a^2$ (Figs. 2, 3) and $S_\ell(\eta)$ (Figs. 4, 5) calculated according to Eqs. 13–15 and Table I, incorporating all terms up to order ϵ^8. These results are exact for $\epsilon^2 = 0$, and can be expected to be quite good for $\epsilon^{10} \ll 1$. As $\epsilon^2 \to 1$, however, significant deviations can be expected in some cases. This is most evident for the second-order function on oblate ellipsoids, where comparisons can be made to exact solutions for the surface of a disk. In Fig. 3, the upper solid curve for k^2a^2 is seen to fall well below the exact value of 14.68 for a disk (the upper dashed line) at $\epsilon^2 = 1$. Similarly, the lowermost solid curve in Fig. 5 is significantly above the exact zeroth-order Bessel function solution for a disk shown as the dashed curve.

Perturbation Calculations

To obtain solutions reliable for ϵ^2 near 1, we transform Eqs. 10a, b to the form

$$\nabla_o^2 S(x) + (k^2a^2 - U)\, S(x) = 0\,, \qquad (17)$$

and apply standard perturbation methods solved by successive approximation (reference 16, Eqs. 9.1.15, 9.1.16). The results are functions of the known eigenvalues and eigenfunctions of the unperturbed operator ∇_o^2, and numerical integrals over products of pairs of eigenfunctions and the perturbation operator U.

For the operator ∇_o^2 we use the Laplacians for rods and disks

$$\nabla_o^2 S(\eta) = \frac{d^2 S(\eta)}{d\eta^2} \qquad (18a)$$

for prolate ellipsoids, and

$$\nabla_o^2 S(\rho) = \frac{1}{\rho}\frac{d}{d\rho}\left[\rho \frac{d}{d\rho} S(\rho)\right] \qquad (18b)$$

for oblate ellipsoids. Combining Eqs. 10, 17, and 18, the corresponding perturbation operators are

$$US(\eta) = \frac{(1-\epsilon^2)\eta^2 \nabla_o^2 S(\eta)}{1-\epsilon^2\eta^2} + \frac{\eta(1-\eta^2) + (1-\epsilon^2)\eta(1+\eta^2)}{(1-\epsilon^2\eta^2)^2}\frac{dS(\eta)}{d\eta} \qquad (19a)$$

for prolate ellipsoids, and

$$US(\rho) = (1-\epsilon^2)\left[\frac{\rho^2 \nabla_o^2 S(\rho)}{1-\epsilon^2\rho^2} + \frac{\rho}{(1-\epsilon^2\rho^2)^2}\frac{dS(\rho)}{d\rho}\right] \qquad (19b)$$

for oblate ellipsoids. Note that

$$\lim_{\epsilon^2 \to 1} US(\rho) = 0$$

for oblate ellipsoids, but not for prolate ellipsoids. While oblate ellipsoids become disks in this limit, prolate ellipsoids become rodlike, but never adopt the uniform profile of a true rod. Nevertheless, the perturbation calculations converge perfectly well for prolate ellipsoids near $\epsilon^2 = 1$.

The results of these calculations (incorporating the first

TABLE I
COEFFICIENTS FOR $S_\ell(\eta)$ AND $k_\ell^2 a^2$

ℓ Prolate/Oblate	1 Prolate	2 Prolate	2 Oblate
q_0	2.0	6.0	6.0
q_2	0.8	2.86	3.14
q_4	0.349	1.45	1.73
q_6	0.165	0.76	0.985
q_8	0.085	0.411	0.575
q_{10}^R	0.160	0.675	2.25
$^*d_{\ell-2,2} \times 10^2$	NA‡	6.7	−6.7
$d_{\ell-2,4} \times 10^2$	NA	2.5	−3.9
$d_{\ell-2,6} \times 10^2$	NA	1.1	−2.4
$d_{\ell-2,8} \times 10^2$	NA	0.56	−1.5
$d_{\ell+2,2} \times 10$	−1.2	−1.96	1.96
$d_{\ell+2,4} \times 10$	−0.371	−0.89	1.07
$d_{\ell+2,6} \times 10$	−0.139	−0.44	0.62
$d_{\ell+2,8} \times 10$	−0.062	−0.23	0.37
$d_{\ell+4,4} \times 10^2$	2.25	1.08	1.07
$d_{\ell+4,6} \times 10^2$	2.07	1.02	1.13
$d_{\ell+4,8} \times 10^2$	1.43	0.77	0.94
$d_{\ell+6,6} \times 10^4$	−1.6	−4.3	4.4
$d_{\ell+6,8} \times 10^4$	−1.3	−5.8	7.2
$d_{\ell+8,8} \times 10^5$	−1.8	0.99	1.23

$^*d_{n,2h} = 0$ for $2h < |n - m|$.
‡NA, not applicable.

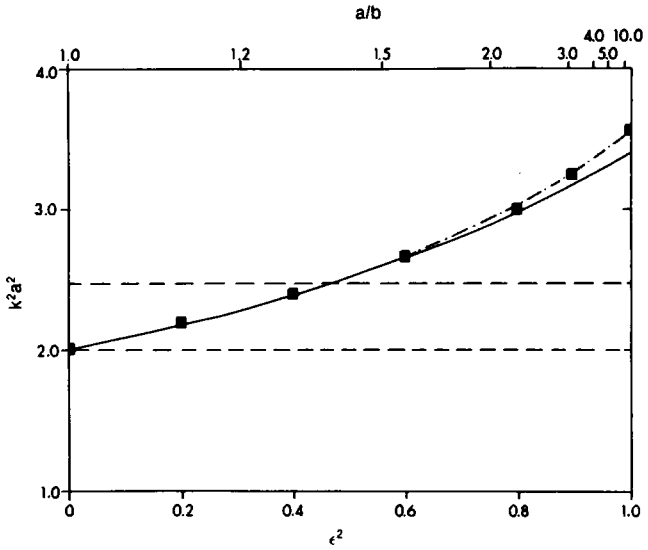

FIGURE 2 Eigenvalues for first-order characteristic function on the surface of a prolate ellipsoid as function of eccentricity ϵ and the corresponding major to minor axial ratio $a/b = (1-\epsilon^2)^{-1/2}$. —, expansion in powers of ϵ^2 according to Eq. 15 and Table I, including terms up to the order of ϵ^8. ■, perturbation calculation based on Fourier series solution for a rod (Eqs. 18a, 19a). –·–, expansion in powers of ϵ^2 adding residual ϵ^{10} term with coefficient q_{10}^R (see Table I) chosen to give the same $\epsilon^2 = 1$ intercept as the perturbation calculation. - - -, limiting values for a sphere and a rod; 2.0 and $(\pi/2)^2$ respectively.

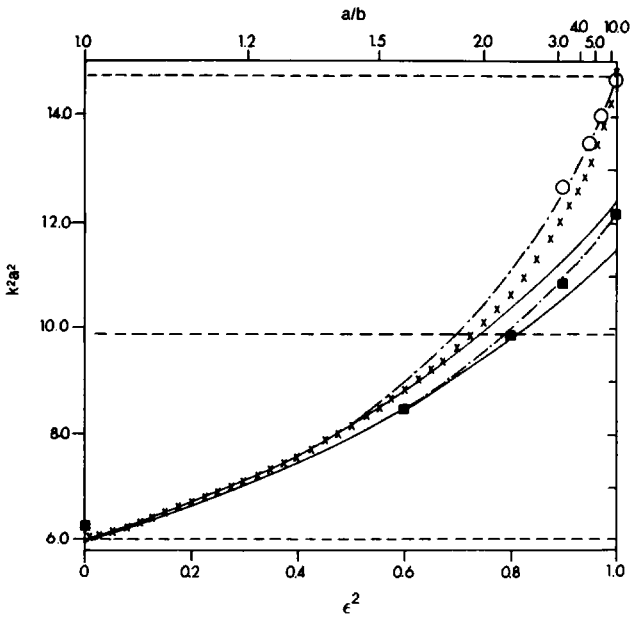

FIGURE 3 Eigenvalues for second-order characteristic functions on the surfaces of prolate and oblate ellipsoids. —, expansion in powers of ϵ^2 according to Eq. 15 and Table I, including terms up to the order of ϵ^8 for oblate (*top*) and prolate (*bottom*) ellipsoids. O, perturbation calculation for oblate ellipsoids based on zeroth-order Bessel function solution for a disk (Eqs. 18b, 19b). ■, perturbation calculation for prolate ellipsoids based on Fourier series solution for a rod (Eq. 18a, 19a). –·–, expansions in powers of ϵ^2 adding residual ϵ^{10} terms with coefficients q_{10}^R (see Table I) chosen to give the exact $\epsilon^2 = 1$ intercept for the oblate ellipsoid, and the same $\epsilon^2 = 1$ intercept as the perturbation calculation for the prolate ellipsoid. x, empirical values for oblate ellipsoids calculated according to Eqs. 20. ---, limiting values for a sphere, rod, and disk; 6.0, π^2, and 14.68, respectively.

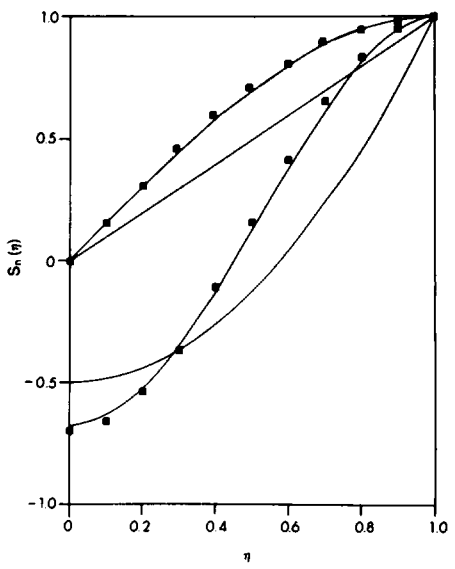

FIGURE 4 First- and second-order eigenfunctions for prolate ellipsoids. —, Legendre polynomial expansions calculated according to Eqs. 13 and 14 and Table I, incorporating terms up to order ϵ^8. The *top* two curves are first-order functions for $\epsilon^2 = 1$ (*top*), and $\epsilon^2 = 0$ (*bottom*). For these functions, one would have $S_1(-\eta) = -S_1(\eta)$. The *bottom* two curves are second-order functions for $\epsilon^2 = 1$ (*top*) and $\epsilon^2 = 0$ (*bottom*). For these functions, $S_2(-\eta) = S_2(\eta)$. ■, corresponding results of perturbation calculations based on Fourier series solution for a rod (Eq. 18a, 19a). All functions are normalized to give $S_n(\eta) = 1$ at $\eta = 1$.

10 to 20 eigenfunctions and eigenvalues of ∇_o^2, and carried through to the fifth-, sixth- or seventh-order approximation, depending upon conditions) are shown in Figs. 2–4. The results for prolate ellipsoids (the ■'s in Figs. 2–4) are seen to be in reasonably good agreement with the corresponding results of the Legendre polynomial expansion (the solid curves) over the entire range of ϵ^2. The deviations between the values for k^2a^2 that do exist near $\epsilon^2 = 1$ can be largely incorporated into residual terms, $q_{10}^R\epsilon^{10}$, added onto the power series expansions (see Table I for values of q_{10}^R). The results including this residual term (shown as –·– in Figs. 2 and 3) are upper bounds for k^2a^2.

Note that empirically, k^2a^2 for oblate ellipsoids is nearly equal to the decay rate that one would have on the surface of a sphere with equal circumferential contour ($2L$), i.e.,

$$k_n^2a^2 = n(n+1)\,(\pi a/L)^2\,, \tag{20a}$$

with

$$L/a = E(\pi\backslash\sin^{-1}\epsilon)\,, \tag{20b}$$

where $E(\Theta\backslash\delta)$ is the elliptic integral of the second kind (21)

$$E(\Theta\backslash\delta) = \int_o^\Theta (1 - \sin^2\delta\sin^2\Theta')^{1/2}d\Theta'\,. \tag{20c}$$

The x's in Fig. 3 are values of $k_2^2a^2$ calculated according to Eqs. 20 as a function of ϵ^2. The value is exact, of course, for the limit of a sphere ($\epsilon^2 = 0$). It is also surprisingly accurate for the opposite limit of a disk ($\epsilon^2 = 1$). In fact, this accuracy extends to all higher-order values of $k_n^2a^2$ as well. The first few values of $k_n^2a^2$ (for even values of n) calculated from Eq. 20a with $L = 2a$ are: 14.804, 49.348, 103.631, 177.653, 271.414, ... The corresponding values calculated from boundary conditions on the zeroth-order

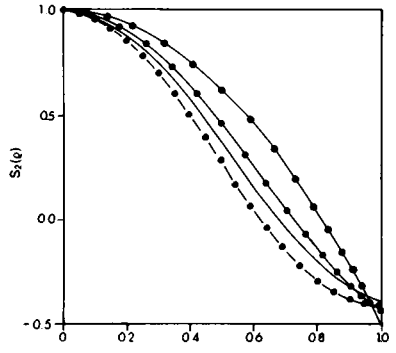

FIGURE 5 Second-order eigenfunctions for oblate ellipsoids. —, Legendre polynomial expansions calculated according to Eqs. 13 and 14 and Table I, incorporating terms up to order ϵ^8, for $\epsilon^2 = 0$ (*top*), $\epsilon^2 = 0.75$ (*middle*), and $\epsilon^2 = 1.0$ (*bottom*). ---, exact zeroth-order Bessel function solution for a disk. ●, corresponding empirical curves calculated according to Eqs. 20, 24a, and 25, for $\epsilon^2 = 0$ (*top*), $\epsilon^2 = 0.75$ (*middle*), and $\epsilon^2 = 1.0$ (*bottom*). All functions are normalized to give $S_2(\rho) = 1$ at $\rho = 0$.

Bessel function for a disk (see above) are: 14.682, 49.219, 103.499, 177.521, 271.282, ...

OTHER DISCOIDAL SURFACES

Consider a general discoidal surface of radius a centrosymmetric about the mid-plane perpendicular to the axis of symmetry (see Fig. 1 *d*). We can map out the surface with two coordinates: $\xi_2 = \lambda$, the normalized ($0 \le \lambda \le 1$) contour distance on the membrane surface measured radially from the top-center; and $\xi_3 = \phi$, the angular coordinate about the axis of symmetry. Correspondingly, we have $h_2 = L$, the contour distance to the bottom-center ($\lambda = 1$) of the disk, and $h_3 = a\rho(\lambda)$, where ρ is the normalized radial coordinate introduced above. In this case, Eq. 3 becomes

$$\frac{d}{d\lambda}\left[\rho(\lambda)\frac{dS(\lambda)}{d\lambda}\right] + k^2L^2\rho(\lambda)S(\lambda) = 0\,. \tag{21}$$

In general, a particular $\rho(\lambda)$ defines a family of possible surface elevation profiles, $z(\rho)$, which can be computed by integration over

$$\frac{dz(\rho)}{d\rho} = \pm a\left[\left(\frac{L}{a}\frac{d\lambda}{d\rho}\right)^2 - 1\right]^{1/2}. \tag{22}$$

We examine now the results for a new specific $\rho(\lambda)$,

$$\rho(\lambda) = [\sin(\pi\lambda)]^{\alpha}\,, \tag{23}$$

a simple analytical form that reduces to that for a sphere at $\alpha = 1$. As shown in Fig. 6, this function generates an interesting series of dimpled discoidal surfaces, ranging from a sphere at $\alpha = 1$ to a closed torus at $\alpha = 2$.

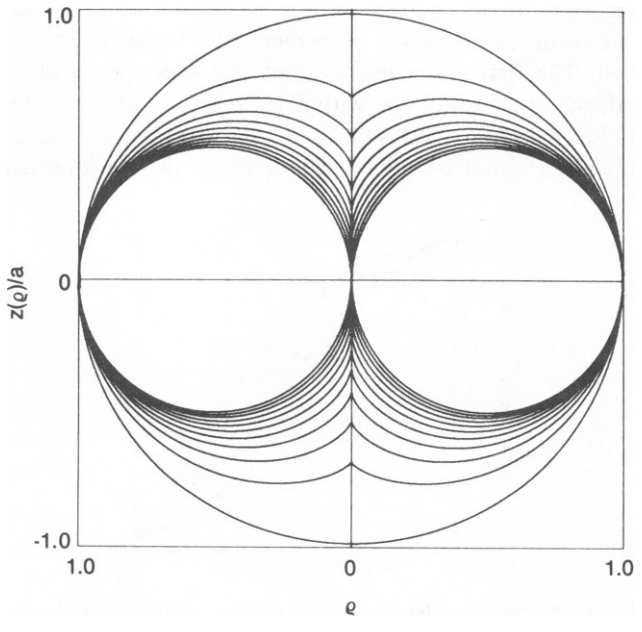

FIGURE 6 A series of cross sections derived by numerical integration over Eq. 22 for surfaces defined by Eq. 23. Values of parameter α range from 1.0 (outermost) to 2.0 (innermost) in equal intervals of 0.1. The minimum possible value of (L/a) (corresponding to the maximum value of $d\rho/d\lambda$) is used in each case.

Combining Eqs. 21 and 23 one can solve for the second-order characteristic function (the first symmetric function after $S_0[\lambda] = 1$), and the corresponding separation constant

$$S_2(\lambda) = 1 - \beta\sin^2(\pi\lambda)\,, \tag{24a}$$

$$k_2^2L^2 = 2\pi^2\beta/(\beta - 1), \tag{24b}$$

where

$$\beta = (2 + \alpha)/(1 + \alpha)\,. \tag{24c}$$

As they must, Eqs. 24 reduce to the known second-order Legendre polynomial solution for a sphere at $\alpha = 1$. Furthermore, combining Eqs. 23 and 24c, it can be verified that

$$\beta = \frac{\int_0^1 \rho(\lambda)d\lambda}{\int_0^1 \sin^2(\pi\lambda)\rho(\lambda)d\lambda}, \tag{25}$$

the precise relationship that must hold for the orthogonality relationship (see Appendix),

$$\int_0^1 S_0(\lambda)S_2(\lambda)\rho(\lambda)d\lambda = 0\,,$$

to be preserved.

Taking Eq. 25 (i.e., the requirement of orthogonality) as defining the value of β, Eqs. 24a and 24b can be used as approximate empirical expressions for other surface geometries.[3] This idea forms the basis of the data analysis methods outlined below for general discoidal surfaces. We can test the accuracy of this approach on oblate ellipsoids, where (L/a) (see Eq. 20), $\rho = \sin\Theta$, and $\lambda = E(\Theta\backslash\sin^{-1}\epsilon)/(L/a)$ can be evaluated explicitly as functions and integrals over equatorial angle $\Theta = \cos^{-1}\eta$ (see Fig. 1 *c*).

Parameter β, calculated according to Eq. 25 by numerical integration, ranges from 1.5 for a sphere at $\epsilon^2 = 0$, to 1.45 for an ellipsoid at $\epsilon^2 = 0.75$, to 1.42 for a disk at $\epsilon^2 = 1$. The corresponding values of $k_2^2a^2$, calculated according to Eqs. 20b, c, and 24b, range from 6.0 at $\epsilon^2 = 0$ (the exact value), to 10.9 at $\epsilon^2 = 0.75$, to 16.6 at $\epsilon^2 = 1$ (a value ~13% too high). The corresponding characteristic functions, calculated according to Eq. 24a, are shown as the solid circles in Fig. 5. The values of $S_2(\rho)$ calculated in this way are exact for $\epsilon^2 = 0$, in good agreement with the Legendre polynomial expansion for $\epsilon^2 = 0.75$, and remarkably accurate for $\epsilon^2 = 1$.

[3]In the original version of this manuscript, Eq. 24a was presented solely as an empirical, approximate solution of Eq. 21, which was shown to work well for oblate ellipsoids. Thanks are due to an anonymous reviewer for demonstrating that the exact problem (i.e., the form of $\rho[\lambda]$ in Eq. 23) could be found for this solution.

EXPERIMENTAL METHODS AND RESULTS

The optical system for fluorescence photobleaching measurements has been described previously (5, 7). The apparatus is centered about a modified research microscope equipped with a fluorescence vertical illuminator. The input optics of the microscope perform three principal functions: shaping the laser beam profile, scanning the laser beam across the sample when necessary, and switching between the monitoring and bleaching beams. Fluorescence is detected with a thermoelectrically cooled photomultiplier tube and quantitated with photon-counting electronics.

We have developed two alternative experimental approaches. In the first, we measure spatially resolved fluorescence distributions, and compute estimates of $M_\ell(t)$ and k_ℓ^2 by numerical integration. In the second, we obtain estimates of $M_\ell(t)$ from the single trace of fluorescence recovery measured with a stationary laser beam. These are considered in turn below.

Fluorescence Redistribution with a Scanning Laser Beam

A servoactivated galvanometric optical scanning mirror controls the precise input angle of the incident beam, and hence the position on the sample of the beam along a scan axis. Uncoated beamsplitters and shutters work in combination to switch between monitoring and bleaching. This arrangement is especially useful for the spatially resolved normal-mode analysis. Because the bleaching and monitoring beams are physically separated between the two beamsplitters, either beam can be selectively modified without affecting the other. Thus, the profile of the bleaching beam can be shaped (e.g., defocused to a line or a diffuse spot) to best produce the spatial distribution of a particular characteristic function. Monitoring is performed as a series of linear scans with a tightly focused spot for maximum spatial resolution. Alternatively, one can illuminate the sample uniformly and record fluorescence images with a low–light-level image-intensified video camera (22).

Values of $c(x, t)$, $d\lambda/dx$, $\lambda(x)$, and L are estimated from experimental values of $F(x, -)$ and $F(x, t)$, the fluorescence intensity at position x along the linear scan axis before bleaching and at time t after bleaching, respectively. These are combined to calculate $M_2(t)$ and k_2^2 according to the empirical methods of the section entitled Other Discoidal Surfaces. Data analysis is based on the following assumptions.

(*a*) The fluorescence recorded within an incremental distance dx along the scan axis is proportional to the product of the concentration of intact fluorophore at that

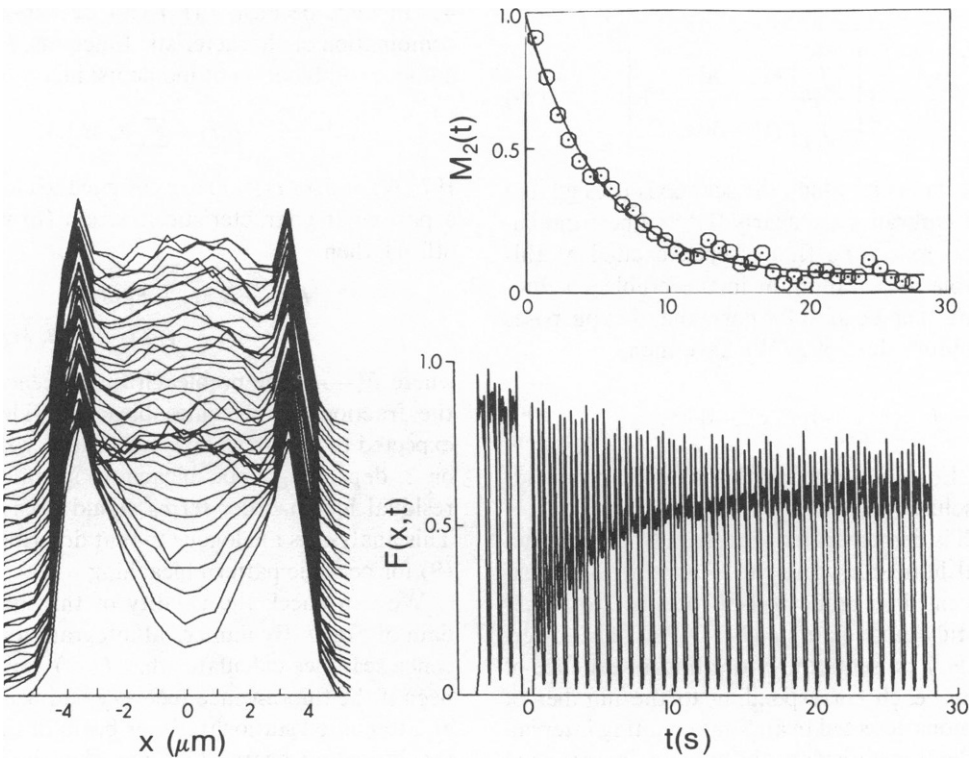

FIGURE 7 Fluorescence photobleaching data for a human erythrocyte labeled with NBD–PE (T = 18°C). *Left:* Stack of individual 24-point fluorescence scans recorded at 0.768 s intervals before and after bleaching. *Lower right:* Linear sequence of the same data as recorded as a function of time. *Upper right:* Normalized values of $M_2(t)$ calculated according to Eqs. 24a, 25, 27, and 29 for each scan (O). The corresponding solid curve is the nonlinear least-squares best fit to an exponential plus a constant.

point times the incremental change of membrane contour length within dx, i.e.,

$$F(x, t)\mathrm{d}x \,\alpha\, c(x, t) \left| \frac{\mathrm{d}\lambda}{\mathrm{d}x} \right| \mathrm{d}x \,. \tag{26}$$

This would not necessarily be true, because of polarization effects, if the order parameters of the absorption and/or emission transition dipoles, relative to a vector perpendicular to the membrane surface, are not nearly zero (see, for example, Fig. 2 of reference 18). To minimize deviations from Eq. 26, the polarization of the incident laser beam is set perpendicular to the scan axis, and hence is very nearly in the plane of the membrane all along the scan, regardless of membrane curvature at the edges. Combining Eqs. 4, 21, and 26, we have (within a constant of proportionality)

$$\begin{aligned} M_2(t) &= \int_{-\infty}^{\infty} c(x, t) S_2(\lambda) \rho(x) \left| \frac{\mathrm{d}\lambda}{\mathrm{d}x} \right| \mathrm{d}x \\ &= \int_{-\infty}^{\infty} F(x, t) S_2(\lambda) \rho(x)\, \mathrm{d}x \,. \end{aligned} \tag{27}$$

(*b*) The concentration of fluorescent label is uniform initially, before bleaching; so that, from Eq. 26

$$F(x, -)\mathrm{d}x \,\alpha \left| \frac{\mathrm{d}\lambda}{\mathrm{d}x} \right| \mathrm{d}x \,. \tag{28}$$

This allows us to compute λ as a function of x along the scan axis

$$\left| \lambda(x) - \frac{1}{2} \right| = \frac{1}{2} \left| \frac{2\int_{-\infty}^{x} F(x', -)\mathrm{d}x'}{\int_{-\infty}^{\infty} F(x', -)\mathrm{d}x'} - 1 \right| . \tag{29}$$

(*c*) At at least one point along the scan axis (designated as $x = x_o$), the membranes are nearly flat and perpendicular to the optical axis. The fluorescence excited at this point, recognizable as a minimum in the prebleach fluorescence scan, can then be used for normalization purposes to calculate absolute values of L. We have then,

$$L = \int_{-\infty}^{\infty} [F(x, -)/F(x_o, -)]\, \mathrm{d}x \,. \tag{30}$$

Combined with Eqs. 24b and 25, this relationship yields the required absolute values of k_2^2.

This approach is demonstrated with data from an intact normal discoidal human erythrocyte labeled with the exogenous fluorescent lipid probe *N*-4-nitrobenzo-2-oxa-1,3-diazole phosphatidylethanolamine (NBD-PE). The lower-right inset to Fig. 7 presents the entire linear sequence of 1,008 data points, each corresponding to the number of fluorescence photons detected in an 8-ms counting interval. The left side of the figure displays the data again, arranged this time into a stack of individual 24-point scans recorded at 0.768-s intervals (192-ms scans with 576-ms pauses between scans).

The cell is bleached for 8 ms at the center of the fifth scan with a defocused laser spot, depleting the central region of the surface, and maximizing the initial amplitude of $S_2(\xi)$ (A_2 in Eq. 2) relative to the other coefficients. Fluorescence redistribution back to the central region is seen to occur rapidly after bleaching. By the last scan, the original form of the prebleach distribution is regained almost completely. Values of $M_2(t)$ are calculated for each scan by numerical integration according to Eqs. 24a, 25, 27, and 29. These are plotted in the upper-right corner. The solid curve superimposed is the nonlinear least-squares best fit to an exponential plus a constant corresponding to an apparent 6% immobile component. The decay rate of the exponential (Dk_2^2), combined with k_2^2 calculated according to Eqs. 24b, 25, and 30, gives $D = 1.75 \times 10^{-9}$ cm^2/s.

Fluorescence Recovery with a Stationary Laser Beam

The sample is bleached and monitored with a stationary laser beam of relative intensity profile $I_o(\xi_2)$. $F(t)$, the fluorescence intensity measured as a function of time after bleaching, is a surface integral over the concentration distribution

$$F(t) = \int c(\xi_2, t)\, I_o(\xi_2) h_2 h_3 \mathrm{d}\xi_2 \mathrm{d}\xi_3 \,, \tag{31}$$

a form reminiscent of the definition of moment $M_\ell(t)$ (Eq. 4). In fact, because $I_o(\xi_2)$ can be expressed as a linear combination of characteristic functions, $F(t)$, in general, is a linear combination of moments; i.e.,

$$F(t) = \sum_n B_n M_n(t) \,. \tag{32}$$

If $I_o(\xi_2)$ and/or $c(\xi_2, t)$ are designed to closely approximate a particular characteristic function (to within a constant offset), then

$$\begin{aligned} F(t) &= B_o M_o + B_\ell M_\ell(t) \\ &= (1 - \gamma) F(-) + B_\ell M_\ell(t) \,, \end{aligned} \tag{33}$$

where $F(-)$ is the prebleach fluorescence intensity and γ the fraction of molecules bleached. This relationship is expected to be particularly accurate for small ℓ (i.e., $\ell = 1$ or 2, depending upon bleaching symmetry), because all residual higher-order terms would decay rapidly to zero. This analysis is analogous to that described by Smith et al. (9) for periodic pattern bleaching.

We can check the validity of this approach using the data of Fig. 7. By numerical integration over each fluorescence scan, we calculate what $F(-)$ and $F(t)$ would have been if the fluorescence recovery had been monitored with an attenuated stationary laser beam of the same profile as the bleaching beam. This can then be compared to the prediction of Eq. 33, by plugging in the diffusion rate calculated above in the full spatially resolved analysis. For the purpose of this exercise, γ is calculated by numerical integration over pre- and postbleach scans. In actual

practice, γ could be determined by measuring the total fluorescence excited by uniform illumination before and after the photobleaching experiment.

The open circles of Fig. 8 are the simulated values of $F(t)/F(-)$, calculated with a laser beam profile estimated from the initial bleached pattern to be a Gaussian with a 2.65 μm $1/e^2$ radius. The solid curve superimposed on the data is the fit to Eq. 33 calculated with B_2 as the only floating parameter. For comparison, the dashed curve is the fluorescence recovery that would be expected (calculated according to Eq. 12 of reference 6) if the fluorescent probe were free to diffuse with the same diffusion coefficient on an unbounded plane. At short times ($t \ll a^2/4D \approx$ 15s), before probe molecules can diffuse over distances comparable to cellular dimensions, the curves are similar, as expected. At longer times, the cell boundaries introduce the marked differences observed. In the bottom curve of the figure, finally, this hypothetical recovery on an unbounded plane is shown rescaled and shifted to give the same long-time asymptote as the actual data.

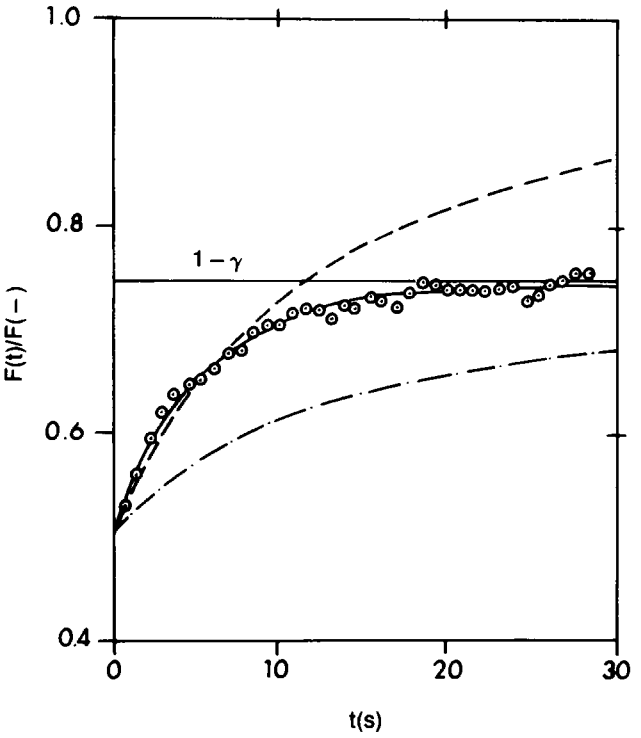

FIGURE 8 Fluorescence photobleaching recovery with a stationary laser beam. O, calculated values of what $F(t)/F(-)$ would have been if the spatially resolved fluorescence redistribution of Fig. 7 had been monitored with an attenuated stationary laser beam of the same profile as the bleaching beam. —, theoretical fit according to simplified theory (Eq. 33), plugging in the diffusion rate calculated in the full analysis of Fig. 7. ---, fluorescence recovery that would be expected if the fluorescent probe were free to diffuse on an unbounded plane. -·-, dot-dashed curve rescaled and shifted for further comparison.

DISCUSSION

The general solution of the equation governing lateral diffusion on a bounded membrane surface is a sum of orthogonal characteristic functions, with the amplitude of each term decaying exponentially with a characteristic decay rate proportional to the diffusion coefficient. In the normal-mode analysis, one imposes an initial concentration distribution approximating one of the lower-order characteristic functions, and follows the subsequent amplitude of that term as a function of time. The initial nonuniform distribution is usually formed by fluorescence photobleaching, but can be formed by other techniques, including membrane fusion (23, 24), electrophoresis (25) and toxin inactivation (26).

The diffusion equations for the surfaces of oblate and prolate ellipsoids of revolution have analytical solutions only in certain limiting cases: the sphere (oblate or prolate ellipsoid as $\epsilon^2 \to 0$), and the disk (oblate ellipsoid as $\epsilon^2 \to 1$). In the analysis above, intermediate cases were solved as Legendre polynomial power series expansions, including terms up to order ϵ^8. Perturbation analysis indicates that these solutions are quite accurate for prolate ellipsoids over the entire range of ϵ^2 ($0 \le \epsilon^2 \le 1$), but are significantly different for oblate ellipsoids from the known analytical solution for disks at $\epsilon^2 = 1$.

The theoretical analyses of surface diffusion rates on ellipsoids produced two surprising results. The rates of redistribution on prolate ellipsoids with ϵ^2 near 1 are larger than those for uniform cross-section rods of equal length (see Figs. 2 and 3). This is true despite the fact that $h_2 d\xi_2$, the length of displacement in the plane of the membrane corresponding to incremental change $d\xi_2$ along the long axis, is always larger for a prolate ellipsoid than it is for the corresponding rod. A detailed analysis indicates that the slowing effect of an increased h_2 can be more than compensated for by h_3, the scale factor incorporating the contour of the cross-section perpendicular to the long axis. Variations in h_3 along the long axis can amplify concentration changes as molecules diffuse through regions of varying area per unit length.

To a remarkable degree, the relaxation rates on an oblate ellipsoidal surface are nearly identical to those characteristic of a sphere with an equatorial circumference equal to the circumference of the ellipse. Applied to the $\epsilon^2 = 1$ limit, this relationship, in fact, leads to an approximate solution for the roots of $dJ_o(x)/dx$ ($x_n = [(2n - 2)(2n - 1)]^{1/2}\pi/2$; $n = 1, 2, \ldots$) considerably better than that given in many texts (e.g., reference 16, p. 1565). Intuitively, one might expect the same relaxation rates from spheres and oblate ellipsoids of equal surface area. The corresponding values, however, are not nearly as accurate as those predicted by the linear circumference.

A simple analytical solution (Eqs. 24) has been found for surface diffusion on a series of dimpled discoids (Fig. 6). This solution, moreover, has been shown to map onto the surfaces of oblate ellipsoids to a surprising degree of accuracy (see Fig. 5). On the basis of these observations, it

is proposed that this solution could serve well as a general one for the analysis of photobleaching data on a variety of discoidal surfaces.

Two alternative experimental approaches implementing the method have been described. The first requires complete, spatially resolved measurements of the evolving fluorescence distribution. The amplitude of the normal mode of interest is computed for each fluorescence scan by numerical integration. All geometrical parameters needed for the analysis are determined from the prebleach scans. The implementation of this approach is relatively difficult technically, but should be facilitated by the current growth of image-intensified digital video technology.

The second approach is much simpler technically, requiring only the measurement of a single trace of fluorescence recovery excited with a stationary laser beam. Fluorescence excitation with suitable monitoring beam profiles optically computes a surface integral approximating that for the normal-mode amplitude. The validity of this approach was demonstrated with a simulated trace of fluorescence recovery (Fig. 8) computed numerically from a set of full spatially resolved fluorescence scans (Fig. 7). The relaxation kinetics of the two analyses were identical within experimental error. Absolute determinations of D from fluorescence recovery kinetics, however, require independent estimates of membrane geometry.

Conventional analysis of localized fluorescence photobleaching recovery experiments assumes an extended membrane geometry, such that the localized depleted area is continuous with an effectively infinite reservoir of unbleached membrane, without interference from membrane boundaries (see Fig. 8). The normal-mode analysis, on the other hand, is designed to work with membranes comparable in size to the depleted area. While this makes the method impractical for very large membranes, it opens the way for the exciting possibility of characterizing cells, vesicles and organelles too small for conventional analysis.

APPENDIX

Orthogonality of Characteristic Functions

Consider the general form of the Liouville equation

$$\frac{d}{dx}\left[p(x)\frac{dS(x)}{dx}\right] + [q(x) + k^2 r(x)]\,S(x) = 0\,, \quad \text{(A1)}$$

with x covering the range $x_1 \le x \le x_2$ (compare with Eq. 3). We wish to examine the conditions necessary to have mutually orthogonal eigenfunctions, i.e.,

$$\int_{x_1}^{x_2} S_i(x)S_j(x)r(x)dx = 0 \text{ (if } i \neq j)\,. \quad \text{(A2)}$$

In the usual way, multiplying Eq. A1 for $S_1(x)$ by $S_2(x)$, multiplying Eq. A1 for $S_2(x)$ by $S_1(x)$, subtracting and integrating over x, it is straightforward to show that Eq. A2 holds for $k_i^2 \neq k_j^2$ if, and only if,

$$p(x_1)\left[S_i(x)\frac{dS_j}{dx} - S_j(x)\frac{dS_i}{dx}\right]_{x=x_1} = p(x_2)\left[S_i(x)\frac{dS_j}{dx} - S_j(x)\frac{dS_i}{dx}\right]_{x=x_2}\,. \quad \text{(A3)}$$

For Eq. 6, condition A3 is true because x_1 and x_2 are the same point. For Eqs. 10a, 10b, 12, and 21, both sides of Eq. A3 are equal to zero. This is true for Eqs. 10a, 10b, and 21 because both end points are singular points [$p(x_1) = p(x2) = 0$] and $S(x)$ is finite. For Eq. 12, x_1 is a singular point, but x_2 is not. Eq. A3 still holds, however, because symmetry dictates that $(dS/dx)_{x=x_2} = 0$.

The author gratefully acknowledges Dr. Arne Bürkli and Peter Febbroriello for technical assistance, Ms. Bridget Clancy-Tenan for typing the manuscript, and the helpful suggestions of an anonymous reviewer.

This work was supported by grant GM23585 from the National Institutes of Health.

Received for publication 10 May 1984 and in final form 20 August 1984.

REFERENCES

1. Cherry, R. 1979. Rotational and lateral diffusion of membrane proteins. *Biochim. Biophys. Acta.* 559:289–327.
2. Jacobson, K. 1980. Fluorescence recovery after photobleaching: lateral mobility of lipids and proteins in model membranes and single cell surfaces. *In* Lasers in Medicine and Biology. F. Hillenkamp, R. Pratesi, and C. Sacchi, editors. Plenum Publishing Corp., New York. 271–288.
3. Peters, R. 1981. Translational diffusion in the plasma membranes of single cells as studied by fluorescence microphotolysis. *Cell Biol. Int. Rep.* 5:733–760.
4. Edidin, M. 1981. Molecular motions and membrane organization and function. *In* Comprehensive Biochemistry, New Series 1, Membrane Structure and Function. M. Florkin and E. H. Stotz, editors. Elsevier/North Holland Biomedical, Amsterdam. 1:37–82.
5. Koppel, D. 1983. Fluorescence photobleaching as a probe of translational and rotational motions. *In* Fast Methods in Physical Biochemistry and Cell Biology. R. I. Sha'afi and S. M. Fernandez, editors. Elsevier/North Holland Biomedical, Amsterdam. 339–367.
6. Axelrod, D., D. E. Koppel, J. Schlessinger, E. L. Elson, and W. W. Webb. 1976. Mobility measurement by analysis of fluorescence photobleaching recovery kinetics. *Biophys. J.* 16:1055–1069.
7. Koppel, D. E. 1979. Fluorescence redistribution after photobleaching. A new multipoint analysis of membrane translational dynamics. *Biophys. J.* 28:281–291.
8. Smith, B. A., and H. M. McConnell. 1978. Determination of molecular motion in membranes using periodic pattern photobleaching. *Proc. Natl. Acad. Sci. USA.* 75:2759–2763.
9. Smith, L. M., J. W. Parce, B. A. Smith, and H. M. McConnell. 1979. Antibodies bound to lipid haptens in model membranes diffuse as rapidly as the lipids themselves. *Proc. Natl. Acad. Sci. USA.* 76:4177–4179.
10. Lanni, F., and B. R. Ware. 1982. Modulation detection of fluorescence photobleaching recovery. *Rev. Sci. Instrum.* 53:905–908.
11. Koppel, D. E., and M. P. Sheetz. 1983. A localized pattern photobleaching method for the concurrent analysis of rapid and slow diffusion processes. *Biophys. J.* 43:175–181.

12. Koppel, D. E., M. P. Sheetz, and M. Schindler. 1980. Lateral diffusion in biological membranes: A normal-mode analysis of diffusion on a spherical surface. *Biophys. J.* 30:187–192.
13. Sheetz, M. P., M. Schindler, and D. E. Koppel. 1980. Lateral diffusion of integral membrane proteins is increased in spherocytic erythrocytes. *Nature (Lond.).* 285:510–512.
14. Koppel, D. E., M. P. Sheetz, and M. Schindler. 1981. Matrix control of protein diffusion in biological membranes. *Proc. Natl. Acad. Sci. USA.* 78:3576–3580.
15. Hochman, J. H., M. Schindler, J. G. Lee, and S. Ferguson-Miller. 1982. Lateral mobility of cytochrome *c* on intact mitochondrial membranes as determined by fluorescence redistribution after photobleaching. *Proc. Natl. Acad. Sci. USA.* 79:6866–6870.
16. Morse, P. M., and H. Feshbach. 1953. Methods of Theoretical Physics. McGraw-Hill, New York. 1978 pp.
17. Huang, H. W. 1973. Mobility and diffusion in the plane of cell membrane. *J. Theor. Biol.* 40:11–17.
18. Smith, L. M., H. M. McConnell, B. A. Smith, and J. W. Parce. 1981. Pattern photobleaching of fluorescent lipid vesicles using polarized laser light. *Biophys. J.* 33:139–146.
19. Olver, F. W. J. 1965. Bessel functions of integral order. *In* Handbook of Mathematical Functions. M. Abramowitz and I. A. Stegun, editors. Dover Publications, New York. 355–433.
20. Crank, J. 1956. The Mathematics of Diffusion. Oxford University Press, London. 76.
21. Milne-Thompson, L. M. 1965. Elliptic integrals. *In* Handbook of Mathematical Functions. M. Abramowitz and I. A. Stegun, editors. Dover Publications, New York. pp. 587–626.
22. Kapitza, H. G., G. McGregor, and K. A. Jacobson. 1984. Application of time resolved spatial photometry (TRSP) to measurement of lateral motion in membranes. *Biophys. J.* 45(2, Pt.2):89*a* (Abstr.)
23. Frye, L. D., and M. Edidin. 1970. The rapid intermixing of cell surface antigens after formation of mouse–human heterokaryons. *J. Cell. Sci.* 7:319–335.
24. Koppel, D. E., and M. P. Sheetz. 1981. Fluorescence photobleaching does not alter the lateral mobility of erythrocyte glycoproteins. *Nature (Lond.).* 293:159–161.
25. Poo, M-m. 1981. *In situ* electrophoresis of membrane components. *Annu. Rev. Biophys. Bioeng.* 10:245–276.
26. Poo, M-m. 1982. Rapid lateral diffusion of functional ACh receptors in embryonic muscle cell membrane. *Nature (Lond.).* 295:332–335.